

Graviton-induced Bremsstrahlung at e^+e^- colliders

Trygve Buanes^{*}, Erik W. Dvergsnes[†], Per Osland[‡]

Department of Physics and Technology, University of Bergen,
Allégaten 55, N-5007 Bergen, Norway

Abstract

We consider graviton-induced Bremsstrahlung at future e^+e^- colliders in both the ADD and RS models, with emphasis on the photon perpendicular momentum and angular distribution. The photon spectrum is shown to be harder than in the Standard Model, and there is an enhancement for photons making large angles with respect to the beam. In the ADD scenario, the excess at large photon perpendicular momenta should be measurable for values of the cut-off up to about twice times the c.m. energy. In the RS scenario, radiative return to graviton resonances below the c.m. energy can lead to large enhancements of the cross section.

^{*}trygve.buanes@ift.uib.no

[†]erik.dvergsnes@ift.uib.no

[‡]per.osland@ift.uib.no

1 Introduction

Early ideas on brane world scenarios date back to more than 15 years ago [1, 2]. In recent years, more predictive and explicit scenarios involving extra dimensions have been proposed [3–7]. As opposed to string theory with tiny compactification scales of $\mathcal{O}(10^{-35} \text{ m})$, there is now a large number of theories which actually will be tested in the current and next generation of experiments.

Here we shall consider two of these scenarios, namely the Arkani-Hamed–Dimopoulos–Dvali (ADD) [3] and the Randall–Sundrum (RS) scenario [6], and investigate some signals characteristic of such models at possible future electron–positron linear colliders like TESLA [8] and CLIC [9].

The most characteristic feature of these models is that they predict the existence of massive gravitons, which may either be emitted into the final state (leading to events with missing energy and momentum), or exchanged as virtual, intermediate states. We shall here focus on the effects of such massive graviton exchange on the Bremsstrahlung process:

$$e^+e^- \rightarrow \mu^+\mu^-\gamma, \quad (1.1)$$

for which the basic electroweak contributions are well known [10].

Due to an extra photon in the final state, this process has a reduced cross section as compared to two-body final states like $\mu^+\mu^-$ and $\gamma\gamma$, and is unlikely to be the discovery channel, but it may provide additional confirmation if a signal should be observed in the two-body final states. In particular, the presence of additional Feynman diagrams, without the infrared and collinear singularities of the Standard Model (SM) leads one to expect a harder photon spectrum.

We shall first, in Sect. 2, present the differential cross section for the process (1.1). Integrated cross sections as well as photon perpendicular momentum and angular distributions will be discussed. Then, in Sects. 3 and 4, we specialize to the ADD and RS scenarios, by performing sums over the respective KK towers. In Sect. 5 we summarize our conclusions.

2 Graviton induced Bremsstrahlung

In this section we present the cross section for the process (1.1), taking into account the s -channel exchange of the photon, the Z and a single graviton of mass $m_{\vec{n}}$ and width $\Gamma_{\vec{n}}$. These results are for the differential cross section very similar to those obtained for graviton exchange in the analogous process $q\bar{q} \rightarrow e^+e^-\gamma$ [11], and will in Sects. 3 and 4 be adapted to the ADD and RS scenarios.

2.1 Differential cross sections

The cross section for the process in Eq. (1.1) is determined by the Feynman diagrams of Fig. 1 (“set A ”, initial state radiation, ISR) and Fig. 2 (“set B ”, final state radiation, FSR), in addition to the well known SM diagrams which are obtained by substituting the

graviton with either a photon or a Z in diagrams (1) and (2) of sets A and B . The SM diagrams are referred to as “sets C_γ ”, “ C_Z ” (both ISR), “ D_γ ”, and “ D_Z ” (both FSR). It is convenient to separate ISR from FSR since, in the case of ISR, the graviton propagator does not carry all the momentum of the electron-positron pair. In fact, this is the reason the two diagrams labeled (4) have been classified as ISR and FSR as given in Figs. 1 and 2.

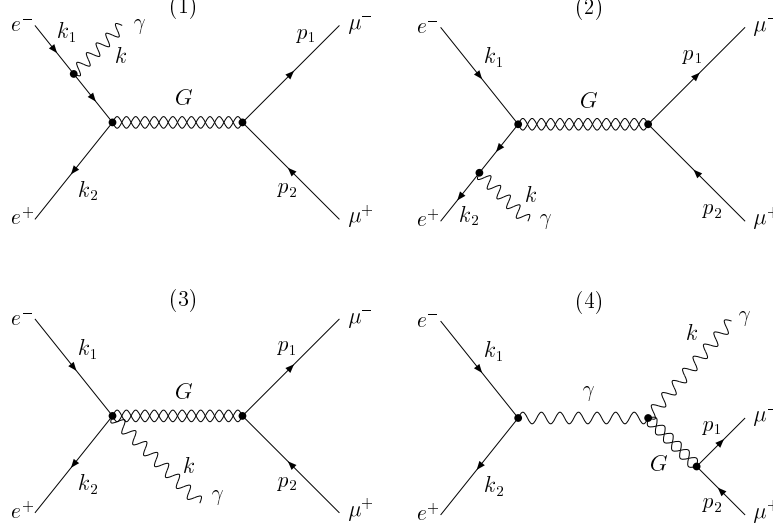


Figure 1: Feynman diagrams for ISR in $e^+e^- \rightarrow \mu^+\mu^-\gamma$. We refer to these diagrams as “set A ”. The corresponding SM diagrams, “set C_γ ” and “set C_Z ”, can be obtained by substituting a photon or a Z for the graviton in diagrams (1) and (2).

We shall here present the different contributions to the differential cross section. Let the incident momenta be k_1 (e^-) and k_2 (e^+), and the outgoing momenta be p_1 (μ^-), p_2 (μ^+) and k (γ), with E_1 , E_2 and ω the corresponding final-state energies. Then, we let x_1 , x_2 and x_3 denote the fractional energies of the muons and the photon

$$x_1 = E_1/\sqrt{s}, \quad x_2 = E_2/\sqrt{s}, \quad x_3 = \omega/\sqrt{s}, \quad 0 \leq x_i \leq \frac{1}{2}, \quad (2.2)$$

with $x_1+x_2+x_3 = 1$. The square of the center of mass energy is $s \equiv (k_1+k_2)^2 = (p_1+p_2+k)^2$ and we denote $s_3 \equiv (p_1+p_2)^2 = (1-2x_3)s$. Furthermore, we let $\eta = x_1 - x_2$.

As shown in Fig. 3, we define the scattering angle θ as the angle between the incoming electron and the outgoing photon. When the polar angle is measured w.r.t. the photon momentum (as in Fig. 3), the forward-backward asymmetry vanishes. This would not be the case if we choose a polar angle referring to a muon momentum.

Following the notation in [11], the different contributions to the cross section are referred to as

$$\sigma_{ee \rightarrow \mu\mu\gamma} = \sigma_{ee \rightarrow \mu\mu\gamma}^{(G)} + \sigma_{ee \rightarrow \mu\mu\gamma}^{(\text{SM})} + \sigma_{ee \rightarrow \mu\mu\gamma}^{(G,\gamma)} + \sigma_{ee \rightarrow \mu\mu\gamma}^{(G,Z)}, \quad (2.3)$$

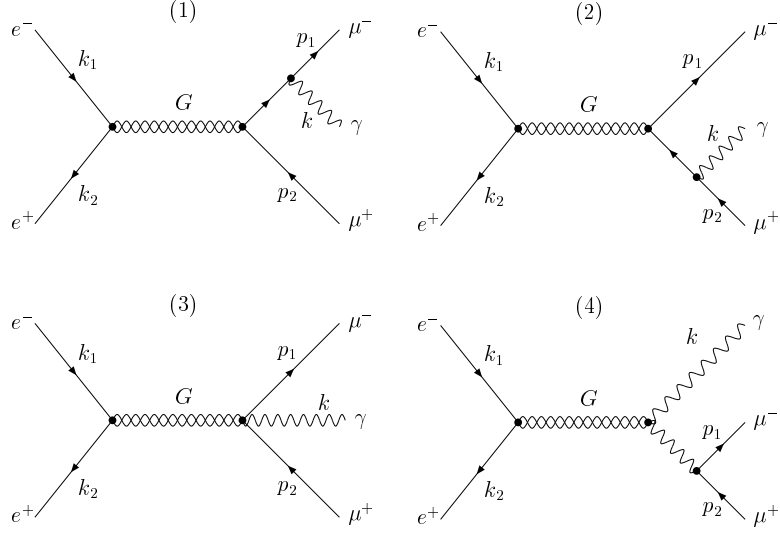


Figure 2: Feynman diagrams for FSR. We shall refer to these as “set B ”. The SM diagrams, “set D_γ ” and “set D_Z ” can be obtained by substituting a photon or a Z for the graviton in diagrams (1) and (2).

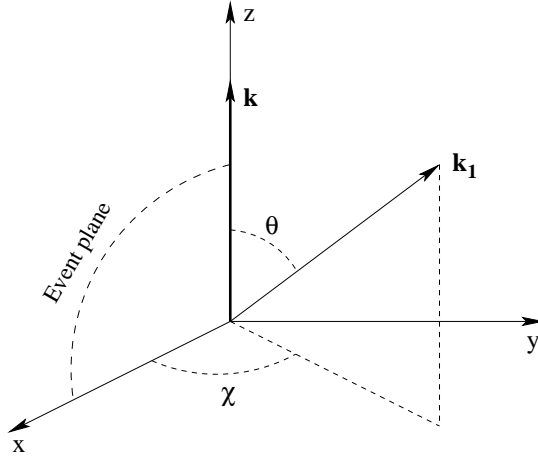


Figure 3: Coordinate frame used to describe $e^+e^- \rightarrow \mu^+\mu^-\gamma$. The incident electron momentum is denoted \mathbf{k}_1 , and \mathbf{k} is the photon momentum.

where the first term is the graviton contribution (sets A and B), the second term is the Standard-model background (sets C and D) and the last two are graviton–photon and graviton– Z interference terms, respectively.

We shall first consider the graviton exchange diagrams, introducing the following notation,

$$\sigma_{ee \rightarrow \mu\mu\gamma}^{(G)} = \sigma_{AA} + \sigma_{AB} + \sigma_{BB}, \quad (2.4)$$

where A and B refer to the initial- and final-state radiation, respectively. The correspond-

ing differential cross section contributions can now be expressed as

$$\begin{aligned}
\frac{d^3\sigma_{AA}}{dx_3 d\eta d(\cos\theta)} &= \frac{\alpha\kappa^4 s Q_e^2}{8192\pi^2} \frac{s_3^2}{(s_3 - m_{\vec{n}}^2)^2 + (m_{\vec{n}}\Gamma_{\vec{n}})^2} X_{AA}(x_3, \eta, \cos\theta), \\
\frac{d^3\sigma_{AB}}{dx_3 d\eta d(\cos\theta)} &= \frac{\alpha\kappa^4 s Q_e Q_\mu}{2048\pi^2} \text{Re} \left[\frac{s_3}{s_3 - m_{\vec{n}}^2 - im_{\vec{n}}\Gamma_{\vec{n}}} \frac{s}{s - m_{\vec{n}}^2 + im_{\vec{n}}\Gamma_{\vec{n}}} \right] X_{AB}(x_3, \eta, \cos\theta), \\
\frac{d^3\sigma_{BB}}{dx_3 d\eta d(\cos\theta)} &= \frac{\alpha\kappa^4 s Q_\mu^2}{8192\pi^2} \frac{s^2}{(s - m_{\vec{n}}^2)^2 + (m_{\vec{n}}\Gamma_{\vec{n}})^2} X_{BB}(x_3, \eta, \cos\theta).
\end{aligned} \tag{2.5}$$

In these expressions, α is the fine-structure constant and $Q_e = Q_\mu = -1$ is the electron and muon charge. (It is convenient to distinguish these, in order to more easily trace the origin of the different terms.) Furthermore, κ denotes the strength of the graviton coupling (to be defined in Sects. 3 and 4 for the ADD and RS scenarios), and $m_{\vec{n}}$ and $\Gamma_{\vec{n}}$ the mass and width of the \vec{n} 'th massive graviton. The angular distributions, as well as the way in which the energy is shared by the muons and the photon, are given by the functions $X_{AA}(x_3, \eta, \cos\theta)$, $X_{AB}(x_3, \eta, \cos\theta)$ and $X_{BB}(x_3, \eta, \cos\theta)$ defined by Eq. (A2) in Appendix A.

The denominator of $X_{BB}(x_3, \eta, \cos\theta)$ [see Eq. (A2)] exhibits the familiar singularities in the infrared and collinear limits, $s_1 \equiv (p_1 + k)^2 = s(1 - 2x_2) \rightarrow 0$, $s_2 \equiv (p_2 + k)^2 = s(1 - 2x_1) \rightarrow 0$, as well as a collinear singularity at $s_3 = s(1 - 2x_3) \rightarrow 0$ due to the fourth Feynman diagram. (Actually, also the ISR contributions in the SM have this singularity, see Eq. (A4), accompanied by a singularity for small angles.) The additional singularity means that there is a tendency to have events with hard photons, like in the analogous hadronic process [11].

The cross sections for the pure SM background is

$$\sigma_{ee \rightarrow \mu\mu\gamma}^{(\text{SM})} = \sigma_{CC} + \sigma_{CD} + \sigma_{DD}, \tag{2.6}$$

where C and D refer to initial- and final-state radiation, with the corresponding contributions to the differential cross section given by

$$\begin{aligned}
\frac{d^3\sigma_{CC}}{dx_3 d\eta d(\cos\theta)} &= \frac{\alpha^3 Q_e^2}{2s} \mathcal{S}_{CC}(s_3, s_3), \\
\frac{d^3\sigma_{CD}}{dx_3 d\eta d(\cos\theta)} &= \frac{2\alpha^3 Q_e Q_\mu}{s} \mathcal{S}_{CD}(s_3, s), \\
\frac{d^3\sigma_{DD}}{dx_3 d\eta d(\cos\theta)} &= \frac{\alpha^3 Q_\mu^2}{2s} \mathcal{S}_{DD}(s, s).
\end{aligned} \tag{2.7}$$

Here, the angular and energy distributions are given by

$$\begin{aligned}
\mathcal{S}_{CD}(s_3, s) &= Q_e^2 Q_\mu^2 X_{C_\gamma D_\gamma}(x_3, \eta, \cos\theta) \\
&+ Q_e Q_\mu \text{Re} \chi(s) X_{C_\gamma D_Z}(x_3, \eta, \cos\theta) + Q_e Q_\mu \text{Re} \chi(s_3) X_{C_Z D_\gamma}(x_3, \eta, \cos\theta) \\
&+ \text{Re}[\chi^*(s_3)\chi(s)] X_{C_Z D_Z}(x_3, \eta, \cos\theta),
\end{aligned} \tag{2.8}$$

with $\mathcal{S}_{CC}(s_3, s_3)$ and $\mathcal{S}_{DD}(s, s)$ similarly obtained from Eq. (2.8) by substituting $(D, s) \leftrightarrow (C, s_3)$. Furthermore, the $X_{C_\gamma D_\gamma}$ etc. are given by Eq. (A4) and the Z propagator is represented by

$$\chi(s) = \frac{1}{\sin^2(2\theta_W)} \frac{s}{(s - m_Z^2) + im_Z\Gamma_Z}, \quad (2.9)$$

with m_Z and Γ_Z the mass and width of the Z boson, and θ_W the weak mixing angle. Note that $\sigma_{C_\gamma C_Z} = \sigma_{C_Z C_\gamma}$ and $\sigma_{D_\gamma D_Z} = \sigma_{D_Z D_\gamma}$.

For the interference terms between graviton exchange and the SM diagrams, we introduce the following notation:

$$\begin{aligned} \sigma_{ee \rightarrow \mu\mu\gamma}^{(G,\gamma)} &= \sigma_{AC_\gamma} + \sigma_{BD_\gamma} + \sigma_{AD_\gamma} + \sigma_{BC_\gamma}, \\ \sigma_{ee \rightarrow \mu\mu\gamma}^{(G,Z)} &= \sigma_{AC_Z} + \sigma_{BD_Z} + \sigma_{AD_Z} + \sigma_{BC_Z}. \end{aligned} \quad (2.10)$$

Like above, the subscripts indicate the diagram sets involved. The corresponding differential cross section contributions are given by

$$\begin{aligned} \frac{d^3\sigma_{AC_\gamma}}{dx_3 d\eta d(\cos\theta)} &= \frac{\alpha^2 \kappa^2 Q_e^3 Q_\mu}{32\pi} \text{Re} \left[\frac{s_3}{s_3 - m_{\tilde{n}}^2 + im_{\tilde{n}}\Gamma_{\tilde{n}}} \right] X_{AC_\gamma}(x_3, \eta, \cos\theta), \\ \frac{d^3\sigma_{AC_Z}}{dx_3 d\eta d(\cos\theta)} &= \frac{\alpha^2 \kappa^2 Q_e^2}{64\pi} \text{Re} \left[\chi^*(s_3) \frac{s_3}{s_3 - m_{\tilde{n}}^2 + im_{\tilde{n}}\Gamma_{\tilde{n}}} \right] X_{AC_Z}(x_3, \eta, \cos\theta), \\ \frac{d^3\sigma_{BD_\gamma}}{dx_3 d\eta d(\cos\theta)} &= \frac{\alpha^2 \kappa^2 Q_e Q_\mu^3}{32\pi} \text{Re} \left[\frac{s}{s - m_{\tilde{n}}^2 + im_{\tilde{n}}\Gamma_{\tilde{n}}} \right] X_{BD_\gamma}(x_3, \eta, \cos\theta), \\ \frac{d^3\sigma_{BD_Z}}{dx_3 d\eta d(\cos\theta)} &= \frac{\alpha^2 \kappa^2 Q_\mu^2}{64\pi} \text{Re} \left[\chi^*(s) \frac{s}{s - m_{\tilde{n}}^2 + im_{\tilde{n}}\Gamma_{\tilde{n}}} \right] X_{BD_Z}(x_3, \eta, \cos\theta), \\ \frac{d^3\sigma_{AD_\gamma}}{dx_3 d\eta d(\cos\theta)} &= \frac{\alpha^2 \kappa^2 Q_e^2 Q_\mu^2}{128\pi} \text{Re} \left[\frac{s_3}{s_3 - m_{\tilde{n}}^2 + im_{\tilde{n}}\Gamma_{\tilde{n}}} \right] X_{AD_\gamma}(x_3, \eta, \cos\theta), \\ \frac{d^3\sigma_{AD_Z}}{dx_3 d\eta d(\cos\theta)} &= \frac{\alpha^2 \kappa^2 Q_e Q_\mu}{128\pi} \text{Re} \left[\chi^*(s) \frac{s_3}{s_3 - m_{\tilde{n}}^2 + im_{\tilde{n}}\Gamma_{\tilde{n}}} \right] X_{AD_Z}(x_3, \eta, \cos\theta), \\ \frac{d^3\sigma_{BC_\gamma}}{dx_3 d\eta d(\cos\theta)} &= \frac{\alpha^2 \kappa^2 Q_e^2 Q_\mu^2}{128\pi} \text{Re} \left[\frac{s}{s - m_{\tilde{n}}^2 + im_{\tilde{n}}\Gamma_{\tilde{n}}} \right] X_{BC_\gamma}(x_3, \eta, \cos\theta), \\ \frac{d^3\sigma_{BC_Z}}{dx_3 d\eta d(\cos\theta)} &= \frac{\alpha^2 \kappa^2 Q_e Q_\mu}{128\pi} \text{Re} \left[\chi^*(s_3) \frac{s}{s - m_{\tilde{n}}^2 + im_{\tilde{n}}\Gamma_{\tilde{n}}} \right] X_{BC_Z}(x_3, \eta, \cos\theta). \end{aligned} \quad (2.11)$$

The X_{AC_γ} etc. are given in Appendix A.

An overview of the notations used for the different contributions to the cross section is given in Table 1.

		ISR			FSR		
		G	γ	Z	G	γ	Z
I S R	G	AA	AC_γ	AC_Z	AB	AD_γ	AD_Z
	γ		$C_\gamma C_\gamma$	$C_\gamma C_Z$	BC_γ	$C_\gamma D_\gamma$	$C_\gamma D_Z$
	Z			$C_Z C_Z$	BC_Z	$C_Z D_\gamma$	$C_Z D_Z$
F S R	G				BB	BD_γ	BD_Z
	γ					$D_\gamma D_\gamma$	$D_\gamma D_Z$
	Z						$D_Z D_Z$

Table 1: Notation used for different combinations of amplitudes. Compare the labeling of diagrams in Figs. 1 and 2.

2.2 Total cross section

To obtain the total cross section, we integrate the differential cross section presented in Sec. 2.1 within the following limits:

$$\sigma_{ee \rightarrow \mu\mu\gamma} = \int_{-1+c_{\text{cut}}}^{1-c_{\text{cut}}} d(\cos \theta) \int_{x_3^{\min}}^{x_3^{\max}} dx_3 \int_{-x_3+y_{\text{cut}}}^{x_3-y_{\text{cut}}} d\eta \frac{d^3 \sigma_{ee \rightarrow \mu\mu\gamma}}{dx_3 d\eta d(\cos \theta)}. \quad (2.12)$$

Since the detector has a ‘blind’ region very close to the beam pipe, we impose a cut, $|\cos \theta| < 1 - c_{\text{cut}}$, with $c_{\text{cut}} = 0.005$, which translates into a lower bound on $\sin \theta_{\min} \simeq 0.1$ or an angular cut of $\theta_{\min} \simeq 100$ mrad. This cut removes the singularity due to initial-state radiation (recall that θ is the angle between the photon and the incident beam).

The resolution cut, $y_{\text{cut}} = 0.005$, is imposed to exclude collinear events, i.e., by requiring $s_i = (1 - 2x_i)s > y_{\text{cut}} s$. For fixed x_3 , this leads to $|\eta| < x_3 - y_{\text{cut}}$, where $\eta = x_1 - x_2$. The variable x_3 is bounded by the allowed values of s_i , giving $y_{\text{cut}} < x_3 < \frac{1}{2}(1 - y_{\text{cut}}) \equiv x_3^{\max}$.

As a result of the cut on s_i , the minimal photon momentum is $k_{\min} = y_{\text{cut}}\sqrt{s}$. For $\sqrt{s} = 500$ GeV and the chosen value for y_{cut} , this becomes 2.5 GeV. In addition to this cut we shall also require that the photon perpendicular momentum is subject to an absolute cut, $k_{\perp} = k \sin \theta > k_{\perp}^{\min}$. Here we choose $k_{\perp}^{\min} = \xi_{\text{cut}}\sqrt{s}$, with $\xi_{\text{cut}} = 0.005$. For $\sqrt{s} = 500$ GeV, $k_{\perp}^{\min} = 2.5$ GeV, which means that photons with momentum k_{\min} only survive this cut when $\sin \theta = 1$. If $\sin \theta = \sin \theta_{\min}$, only photons of $k > 25$ GeV survive the cuts.

When expressed in terms of the variables x_3 and $\cos \theta$, the k_{\perp} constraint becomes

$x_3\sqrt{1-\cos^2\theta} > \xi_{\text{cut}}$. Thus, for a given $\cos\theta$ in the allowed range, we find

$$x_3 > x_3^{\min} = \max\left(\frac{\xi_{\text{cut}}}{\sqrt{1-\cos^2\theta}}, y_{\text{cut}}\right) \quad (2.13)$$

In order to exclude radiative return to the Z , we will also consider the cut

$$s_3 > (m_Z + 3\Gamma_Z)^2 \equiv y_{\text{cut}}^{\text{rr}} s. \quad (2.14)$$

This implies

$$y_{\text{cut}}^{\text{rr}} = \frac{m_Z^2}{s} \left(1 + \frac{3\Gamma_Z}{m_Z}\right)^2 \simeq 1.17 \times \frac{m_Z^2}{s}, \quad (2.15)$$

which for $\sqrt{s} = 500$ GeV gives $y_{\text{cut}}^{\text{rr}} \simeq 0.039$. This value will modify the upper bound x_3^{\max} , which will become $\frac{1}{2}(1 - y_{\text{cut}}^{\text{rr}})$, but not affect the lower bound, x_3^{\min} , nor the limits on η .

2.3 Photon perpendicular momentum distribution

It is instructive to consider the spectrum of the photon perpendicular momentum, k_{\perp} , since this has no analogue in the two-body final state process. As anticipated above, we expect it to be harder than in the QED case. The relevant differential cross sections can be obtained from the expressions in Sec. 2.1 upon a change of variables from $(x_3, \cos\theta) \rightarrow (k_{\perp}, k_{\parallel})$. From the definitions, $k_{\perp} = \sqrt{s}x_3 \sin\theta$ and $k_{\parallel} = \sqrt{s}x_3 \cos\theta$, we get $dx_3 d(\cos\theta) \rightarrow |J| dk_{\parallel} dk_{\perp}$ with the Jacobian

$$|J| = \frac{k_{\perp}}{\sqrt{s}k^2} = \frac{k_{\perp}}{\sqrt{s}(k_{\perp}^2 + k_{\parallel}^2)}. \quad (2.16)$$

The photon perpendicular momentum spectrum is now obtained from

$$\frac{d\sigma_{ee \rightarrow \mu\mu\gamma}}{dk_{\perp}} = \int_{-k_{\parallel}^{\max}}^{k_{\parallel}^{\max}} dk_{\parallel} \int_{-x_3+y_{\text{cut}}}^{x_3-y_{\text{cut}}} d\eta \frac{d\sigma_{ee \rightarrow \mu\mu\gamma}^3}{dk_{\perp} dk_{\parallel} d\eta}. \quad (2.17)$$

Given some k_{\perp} within the allowed region $\xi_{\text{cut}}\sqrt{s} < k_{\perp} < \frac{\sqrt{s}}{2}(1 - y_{\text{cut}})$, we find

$$|k_{\parallel}| < k_{\parallel}^{\max} = \min\left(\sqrt{\frac{s}{4}(1 - y_{\text{cut}})^2 - k_{\perp}^2}, \frac{\sqrt{s}}{2}(1 - y_{\text{cut}})(1 - c_{\text{cut}})\right). \quad (2.18)$$

The resolution cut, y_{cut} , and also the radiative-return cut, $y_{\text{cut}}^{\text{rr}}$, will be the same as for the total cross section, and the radiative-return cut will affect both k_{\perp}^{\max} and k_{\parallel}^{\max} .

2.4 Photon angular distribution

For the two-body final states $e^+e^- \rightarrow \mu^+\mu^-$ and $e^+e^- \rightarrow \gamma\gamma$, the QED angular distributions are given by the familiar $1 + \cos^2\theta$ and $(1 + \cos^2\theta)/(1 - \cos^2\theta)$. For graviton exchange, the corresponding distributions become $1 - 3\cos^2\theta + 4\cos^4\theta$ and $1 - \cos^4\theta$ (see e.g. [12]). In both these cases, the higher powers are due to the spin-2 coupling. For the three-body

case, we get similar expressions (see the Appendix). Note that the ISR contribution has a structure similar to that of the diphoton channel, with a $1 - \cos^2 \theta$ singularity in the denominator, whereas graviton exchange gives quartic terms in $\cos \theta$.

In order to emphasize the photons originating from graviton exchange over those from the collinear singularities (dominated by the SM contributions), we will here consider the angular distribution of the *photon* with respect to the incident beam:

$$\frac{d\sigma_{ee \rightarrow \mu\mu\gamma}}{d(\cos \theta)} = \int_{x_3^{\min}}^{x_3^{\max}} dx_3 \int_{-x_3+y_{\text{cut}}}^{x_3-y_{\text{cut}}} d\eta \frac{d^3\sigma_{ee \rightarrow \mu\mu\gamma}}{dx_3 d\eta d(\cos \theta)}, \quad (2.19)$$

with the cuts as given above.

3 The ADD scenario

We first turn our attention to the ADD scenario [3], where there is essentially a continuum of massive graviton states up to some cut-off M_S , where a more fundamental theory, presumably low-scale string physics, takes over. Following the convention of [13], the coherent sum over all KK modes in a tower is performed by substituting for the sum over graviton propagators the following expression:

$$\frac{\kappa^2}{s - m_{\vec{n}}^2 + im_{\vec{n}}\Gamma_{\vec{n}}} \equiv -i\kappa^2 D(s) \xrightarrow{\sum_{\vec{n}}} \frac{8\pi s^{n/2-1}}{M_S^{n+2}} [2I(M_S/\sqrt{s}) - i\pi], \quad (3.20)$$

with

$$I(M_S/\sqrt{s}) = \begin{cases} -\sum_{k=1}^{n/2-1} \frac{1}{2k} \left(\frac{M_S}{\sqrt{s}}\right)^{2k} - \frac{1}{2} \log\left(\frac{M_S^2}{s} - 1\right), & n = \text{even}, \\ -\sum_{k=1}^{(n-1)/2} \frac{1}{2k-1} \left(\frac{M_S}{\sqrt{s}}\right)^{2k-1} + \frac{1}{2} \log\left(\frac{M_S + \sqrt{s}}{M_S - \sqrt{s}}\right), & n = \text{odd}. \end{cases} \quad (3.21)$$

for n extra dimensions.

Since the role of higher-order loop effects is rather unknown [14], these expressions should not be taken too literally. However, in order to preserve the qualitative difference between the two propagators $D(s)$ and $D(s_3)$ (see Eq. (3.20)), and thus more easily keep track of the contributions of different Feynman diagrams, we shall use the expressions of Eq. (3.21). In the approach of [15] and [16] the n -dependence is absorbed in the cut-off so that $D(s)$ and $D(s_3)$ are indistinguishable. For $n = 4$ and $M_S \gg \sqrt{s}$, the cut-off M_S is comparable to Λ_T of ref. [15] and M_H of [16].

3.1 Total cross sections

In Figs. 4 and 5, we present the total cross section [see Eq. (2.12)] vs. the UV cut-off M_S , for $n = 2, 4$ and 6 . (For $n = 2$, this range of M_S is actually in conflict with astrophysical

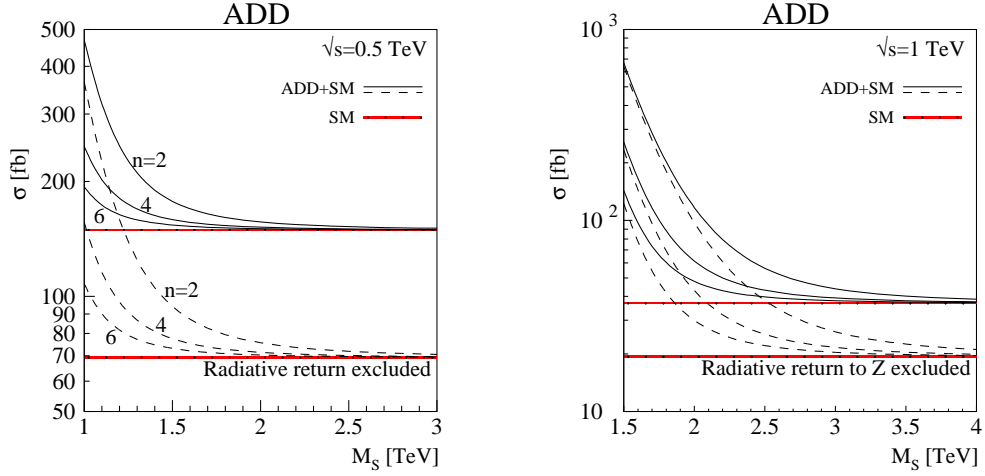


Figure 4: Total cross sections for $e^+e^- \rightarrow \mu^+\mu^-\gamma$ vs. M_S , for $\sqrt{s} = 0.5$ and 1 TeV, and $n = 2, 4$ and 6, with (solid) and without (dashed) radiative return to the Z pole. The SM value is represented by a band corresponding to $\mathcal{L}_{\text{int}} = 300 \text{ fb}^{-1}$.

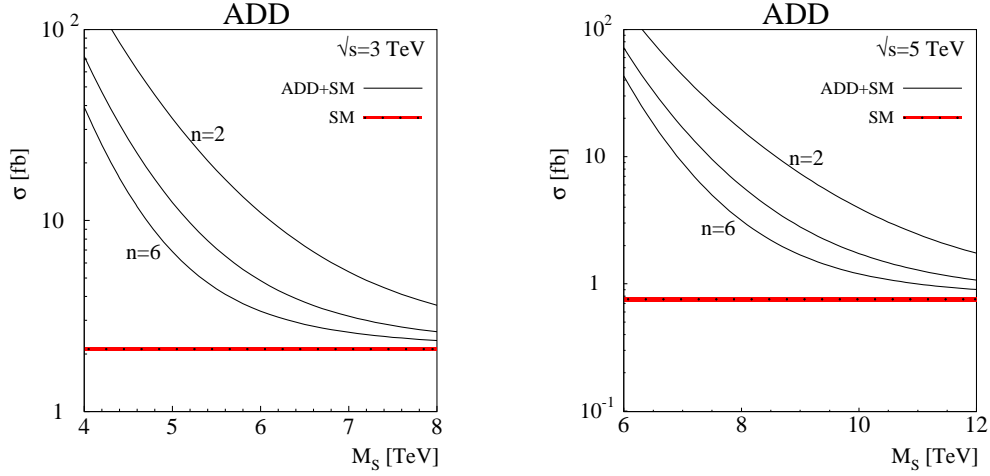


Figure 5: Total cross sections for $e^+e^- \rightarrow \mu^+\mu^-\gamma$ vs. M_S , for $\sqrt{s} = 3$ and 5 TeV, and $n = 2, 4$, and 6. The SM value is represented by a band corresponding to $\mathcal{L}_{\text{int}} = 1000 \text{ fb}^{-1}$.

data [17].) Different collider energies are considered, $\sqrt{s} = 0.5$ and 1.0 TeV in Fig. 4, and 3.0 and 5.0 TeV in Fig. 5. For $\sqrt{s} = 3$ and 5 TeV, radiative return to Z is already excluded by the y cut, and therefore only one set of curves is shown.

It is seen that the integrated cross sections can have a significant enhancement over the SM result provided M_S is not too much above the actual c.m. energy. Also, we note that removing the radiative return to the Z according to the criterion (2.14), the cross section is reduced significantly. Since this mostly affects the SM background, the relative magnitude of the “signal” increases.

As a rough indication of the precision to be expected, we display the 1σ statistical error

band around the SM values, corresponding to an integrated luminosity of 300 fb^{-1} for the cases of $\sqrt{s} = 0.5$ and 1 TeV , and 1000 fb^{-1} for $\sqrt{s} = 3$ and 5 TeV (we take the efficiency to be 1 throughout the paper). We note that the sensitivity of the integrated cross section extends out to values of \sqrt{s} that are a few times the available c.m. energy. However, since it is a higher-order process, suppressed by a factor of the order α/π , the sensitivity does not compete with that of the two-body final states [16, 18, 19].

3.2 Photon perpendicular momentum distributions

Because of the Feynman diagrams (3) and (4), the photon tends to be harder than in QED or the SM [11]. This is illustrated in Fig. 6 for $\sqrt{s} = 0.5 \text{ TeV}$, where we show $d\sigma_{ee \rightarrow \mu\mu\gamma}/dk_{\perp}$ as given by Eq. (2.17) for $n = 4$ and $M_S = 1.5 \text{ TeV}$. The peak at the highest values of $k_{\perp} \sim \frac{1}{2}\sqrt{s}$ is due to radiative return to the Z . As can be seen in this figure, radiative return mainly affects the SM background, and can be removed by a cut on s_3 [see Eq. (2.14)].

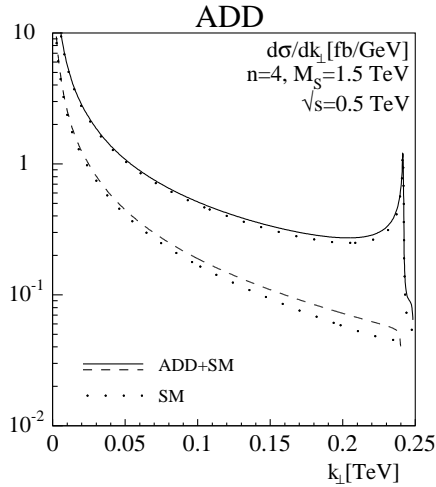


Figure 6: Photon perpendicular momentum distribution for $n = 4$, with (upper) and without (lower curve) radiative return to Z . The SM contribution is dotted.

In order to give an idea how significant the difference is, we also show in Figs. 7 and 8 bin-integrated k_{\perp} distributions, corresponding to an integrated luminosity of 300 fb^{-1} for 0.5 and 1 TeV , with a bin width of 50 GeV , and an integrated luminosity of 1000 fb^{-1} for 3 and 5 TeV , with a bin width of 100 GeV . In these figures, we have taken $n = 4$ and selected values of M_S , namely $1.5, 3, 8$ and 12 TeV .

It is seen that, after the binning in k_{\perp} , the excess of the ADD+SM cross section over the SM cross section remains significant for the considered luminosities. As anticipated, the excess increases with k_{\perp} , also with respect to the statistical uncertainty, in particular after the removal of radiative-return events. The quantitative benefit of this radiative-return cut will of course depend on the integrated luminosity and the cut parameter [see Eq. (2.14)] as well as on M_S . As mentioned above, for $\sqrt{s} = 3$ and 5 TeV , radiative return to Z is already excluded by the y cut, thus only one set of curves is displayed.

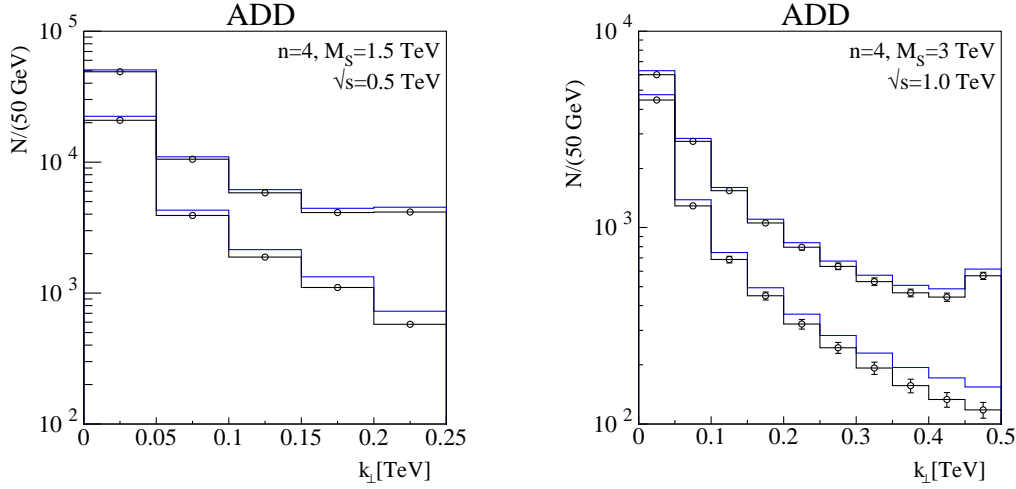


Figure 7: Photon perpendicular momentum distributions for $n = 4$, with (upper) and without (lower set of curves) radiative return to Z . The SM contribution is displayed with error bars (invisible in the left panel) corresponding to 300 fb^{-1} .

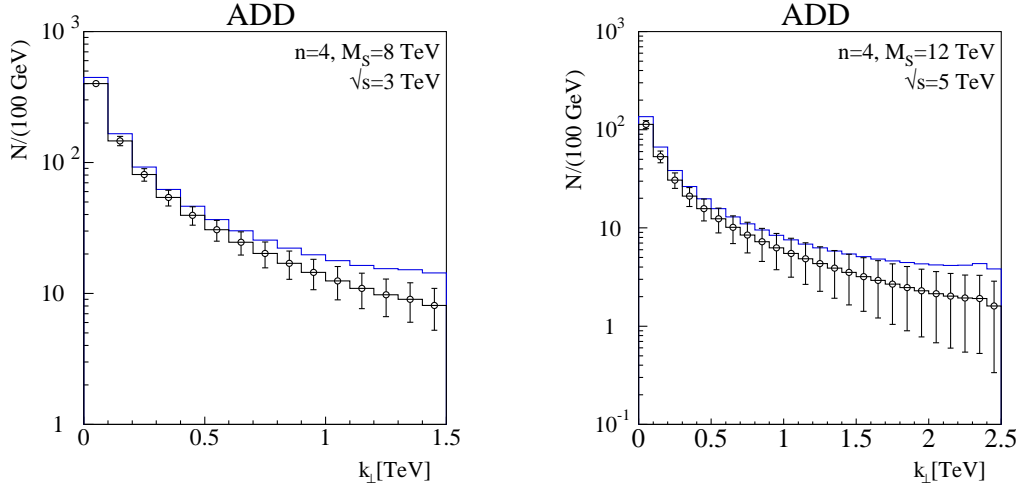


Figure 8: Photon perpendicular momentum distributions for $n = 4$. The SM contribution is displayed with error bars corresponding to 1000 fb^{-1} .

3.3 Photon angular distributions

Due to conventional ISR (diagrams (1) and (2) in Fig. 1), the photon angular distributions are peaked near the beam direction. This is the case for any s -channel exchange, and stems from the collinear singularity of those diagrams. Similarly, diagrams (1) and (2) in Fig. 2 (final-state radiation) lead predominantly to photons close to the directions of the final-state muon momenta. On the other hand, the diagrams (3) and (4), for ISR as well as for FSR, do not have such collinear singularities, and could therefore lead to distinctive features, different from those of the SM.

We show in the left panel of Fig. 9 the photon angular distribution for $\sqrt{s} = 0.5 \text{ TeV}$,

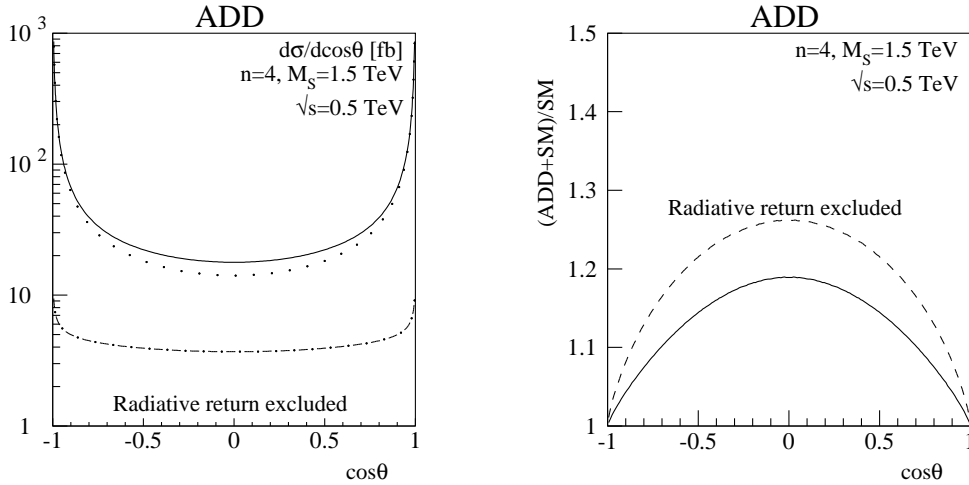


Figure 9: Photon angular distribution for $\sqrt{s} = 0.5$ TeV. Left panel: SM (dotted), contributions with graviton-exchange involved (dash-dotted), ADD+SM (solid). Radiative return to the Z pole is excluded. Right panel: Ratio $(\text{ADD}+\text{SM})/\text{SM}$, with (solid) and without (long-dashed) radiative return to the Z pole.

$M_S = 1.5$ TeV and $n = 4$, where radiative return to the Z has been excluded. As suggested by the above discussion, the effect of the graviton exchange is mostly to increase the distribution in the central region, i.e., for photons making large angles with the beams.

The enhancement at large angles, with respect to the SM, is more clearly seen in the right panel of Fig. 9, where we show the ratio, $(\text{ADD}+\text{SM})/\text{SM}$, with and without radiative return to the Z . For the parameters chosen, there is for photons perpendicular to the beam, and for the considered parameters, an enhancement of about 25%.

4 The RS scenario

The phenomenology of the RS scenario [6] differs from that of the ADD scenario in several respects. This scenario has two 3-branes separated in the fifth dimension, and a non-factorisable geometry, which means that the four-dimensional metric depends on the coordinate in the fifth dimension. It gives rise to a tower of massive KK gravitons with the mass of the n 'th resonance related to that of the first one, m_1 , in the following way [20]

$$m_n = \frac{x_n}{x_1} m_1, \quad (4.22)$$

where x_n are zeros of the Bessel function $J_1(x_n) = 0$, with $x_1 \simeq 3.83$ (not to be confused with the energy fraction carried by the μ^- , also denoted x_1). Therefore the mass splittings in the RS model are non-equidistant. The mass of the first resonance is assumed to be of the order of TeV, so only a few resonances are within reach of collider experiments. In Fig. 10 we show the lowest states for a range of m_1 values. Since there are only a few graviton resonances kinematically available, the summation over them is straightforward.

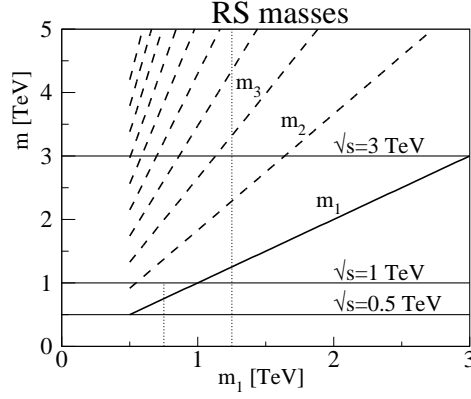


Figure 10: The lowest masses m_i vs. m_1 , for the RS scenario. The vertical (dotted) lines correspond to values of m_1 considered in Figs. 13 and 14. The horizontal lines correspond to c.m. energies considered.

The RS scenario can for our purposes be parametrized by two parameters, the mass of the lowest massive graviton, m_1 , and $k/\overline{M}_{\text{Pl}}$, a dimensionless quantity typically taken in the range 0.01–0.1, effectively giving the strength of the graviton coupling [20]. The parameter k here refers to the curvature of the five-dimensional space, and should not be confused with the photon momentum, also denoted k .

Expressed in terms of RS parameters, the graviton coupling, κ , of Eqs. (2.5) and (2.11) becomes

$$\kappa = \sqrt{2} \frac{x_1}{m_1} \frac{k}{\overline{M}_{\text{Pl}}}, \quad \overline{M}_{\text{Pl}} = \frac{M_{\text{Pl}}}{\sqrt{8\pi}} = 2.4 \times 10^{18} \text{ GeV}, \quad (4.23)$$

and the widths of the resonances are given by (see [13, 21, 11])

$$\Gamma_n = \frac{\gamma_G}{10\pi} x_n^2 m_n \left(\frac{k}{\overline{M}_{\text{Pl}}} \right)^2, \quad (4.24)$$

where $\gamma_G = 295/96$ (for coupling to the SM particles only).

While an RS graviton couples like an ADD graviton (apart from the strength), the overall phenomenology is rather different. For the two-body final states, the RS gravitons, since they are very narrow, only contribute to the cross section if the c.m. energy coincides with a graviton mass. This restriction is lifted for the three-body final states considered here, since the diagrams of Fig. 1 (for ISR) may resonate when s_3 has a suitable value (see Eq. (2.5)), i.e., radiative return may lead to an enhancement of the cross section.

We shall below discuss total cross sections and photon perpendicular-momentum distributions. The angular distributions will not be displayed for the RS case, they are very similar to the distributions shown for the ADD case. If $\sqrt{s} \simeq m_i$, graviton exchange will dominate, which results in a distribution like the dash-dotted one in Fig. 9. If we are far away from any direct resonance, the distribution will be a mixture of the SM and graviton distributions like in the ADD case.

4.1 Total cross sections

In Figs. 11 and 12, we present the total cross sections for the Bremsstrahlung process (1.1) at four different collider energies, $\sqrt{s} = 0.5, 1, 3$ and 5 TeV, as functions of m_1 , and for different values of $k/\overline{M}_{\text{Pl}} = 0.01, 0.05$ and 0.1.

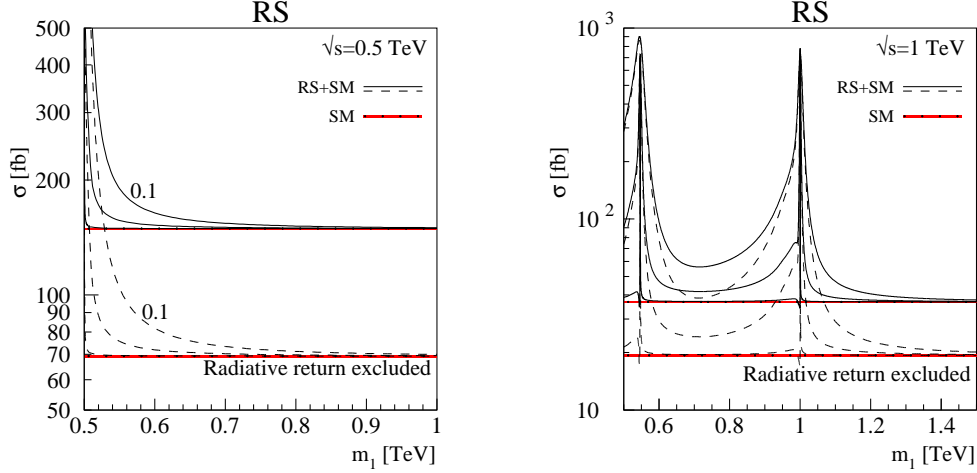


Figure 11: Total cross sections for $e^+e^- \rightarrow \mu^+\mu^-\gamma$ vs. M_S , for $\sqrt{s} = 0.5$ and 1 TeV, with (solid) and without (dashed) radiative return to the Z pole. Three values of $k/\overline{M}_{\text{Pl}}$ are considered for each energy; from top and down: 0.1, 0.05 and 0.01. The SM contribution is represented by a band corresponding to 300 fb^{-1} .

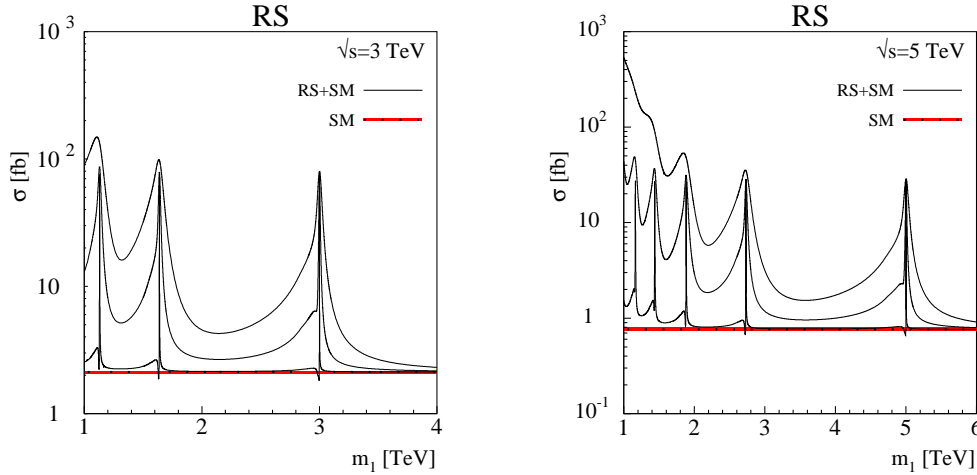


Figure 12: Total cross sections for $e^+e^- \rightarrow \mu^+\mu^-\gamma$ vs. M_S , for $\sqrt{s} = 3$ and 5 TeV. Three values of $k/\overline{M}_{\text{Pl}}$ are considered, like in Fig. 11. The SM contribution is represented by a band corresponding to 1000 fb^{-1} .

Some of these figures have a lot of structure. Anticipating that values of m_1 below the lowest considered c.m. accelerator energy will already be excluded, we show in Fig. 11 for

$\sqrt{s} = 0.5$ TeV (left panel) only values of m_1 such that $m_1 > \sqrt{s}$. However, if the resonance is reasonably broad (high $k/\overline{M}_{\text{Pl}}$), there can be a considerable increase of the cross section for some range of m_1 values well above the c.m. energy. Like for the ADD case, exclusion of radiative return to the Z leads to an improvement of the signal.

At the next higher energy studied, $\sqrt{s} = 1$ TeV (Fig. 11, right panel), we consider a range of m_1 values, below the c.m. energy, as well as above. Apart from the obvious resonance peak when $m_1 \simeq \sqrt{s}$, there is also a sharp peak for values of m_1 around 0.55 TeV. From Fig. 10 we see that this corresponds to the second graviton, with mass m_2 , being produced resonantly. We shall refer to both these cases as “direct” resonances, since $\sqrt{s} = m_i$ for some i .

In Fig. 12, this phenomenon of producing higher resonances is demonstrated for the c.m. energies of 3 and 5 TeV. In the right panel of Fig. 12, for $\sqrt{s} = 5$ TeV, we see for $m_1 \simeq 1$ TeV and large $k/\overline{M}_{\text{Pl}}$ an enhancement of the cross section by more than two orders of magnitude. This is in part caused by the higher resonances being close to each other (and wide), such that several of them can interfere. Also radiative return to lower states contributes, as discussed below.

In this same panel, we note that there is a significant enhancement of the RS cross section in the region around $m_1 = 4$ TeV, which is not compatible with any direct resonance (when $\sqrt{s} = 5$ TeV). This enhancement is more than what can be attributed to the width of the nearby resonances, it is caused by diagrams where the s_3 -channel may resonate, i.e., where $\sqrt{s_3} \simeq m_1$ and the remaining energy is carried by the photon.

4.2 Photon perpendicular momentum distributions

In the photon perpendicular-momentum distribution, we expect a harder spectrum than in the SM case, as was the case for the ADD scenario. Furthermore, resonant production of either the lowest (m_1) or a higher resonance (m_i) can lead to a sharp edge for

$$k_{\perp} \lesssim \frac{s - m_i^2}{2\sqrt{s}}, \quad (4.25)$$

characteristic of radiative return to a lower state, $m_i < \sqrt{s}$.

Fig. 13 is devoted to k_{\perp} distributions for $\sqrt{s} = 1$ TeV, two values of m_1 , and $k/\overline{M}_{\text{Pl}} = 0.05$. The higher curves in the left panel show k_{\perp} distributions for a reasonably low value of m_1 , chosen such that the second resonance coincides with the c.m. energy. The distribution is for all k_{\perp} higher than that of the SM by more than one order of magnitude, the excess increasing with k_{\perp} . The small structure at $k_{\perp} \sim 0.35$ TeV is due to radiative return to the lower resonance at $m_1 \simeq 0.55$ TeV, with the “resonant” k_{\perp} given by Eq. (4.25). The lower curves in the left panel correspond to a value of $m_1 = 0.75$ TeV for which there is no direct resonance. Hence, the indirect effect of radiative return becomes more visible, there is a distinct enhancement at the value of k_{\perp} corresponding to (4.25).

In the right panel we show the binned distribution for $m_1 = 0.75$ TeV together with the SM prediction with error bars corresponding to $\mathcal{L}_{\text{int}} = 300 \text{ fb}^{-1}$. The bin width has been

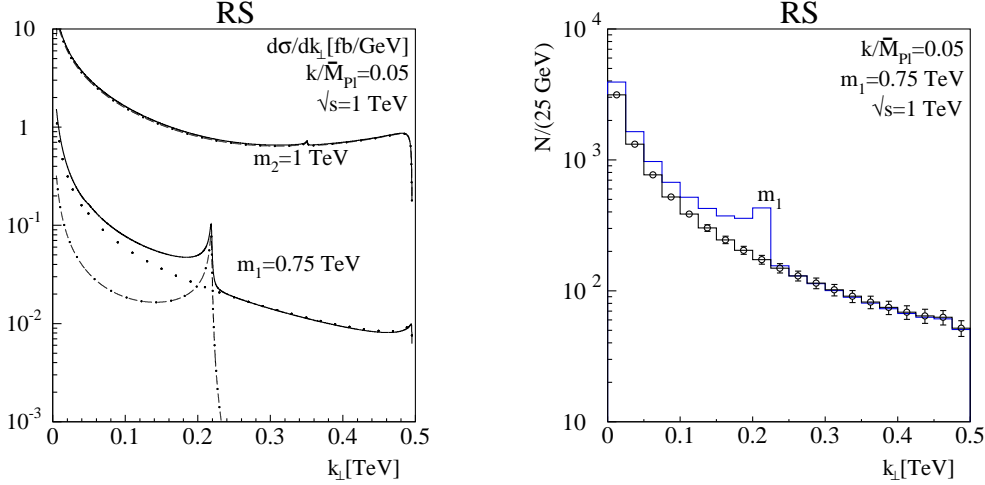


Figure 13: Photon perpendicular momentum distributions for $\sqrt{s} = 1 \text{ TeV}$. Radiative return to the Z is excluded. Left panel: Two values of m_1 are considered, lower curves, $m_1 = 0.75 \text{ TeV}$, upper curve: $m_1 \simeq 0.55 \text{ TeV}$ chosen such that $m_2 = 1 \text{ TeV}$. The graviton-related contributions are dash-dotted, the SM contribution is dotted. Right panel: Bin-integrated k_\perp distribution for $m_1 = 0.75 \text{ TeV}$. The SM distribution is shown with error bars corresponding to $\mathcal{L}_{\text{int}} = 300 \text{ fb}^{-1}$.

chosen as 25 GeV [8]. The enhancement related to radiative return to the m_1 is clearly visible above the statistical noise.

In Fig. 14 we show k_\perp distributions for $\sqrt{s} = 5 \text{ TeV}$ and two values of m_1 . The upper curves in the left panel correspond to a value of m_1 for which there is a direct resonance corresponding to $m_5 = \sqrt{s}$. The spectrum is very hard, and small features corresponding to radiative return to all the lower resonances are seen. The middle curves, which are about an order of magnitude above the SM background (dotted), correspond to a value $m_1 = 1.25 \text{ TeV}$ for which there is no direct resonance. As can be seen from Fig. 10, m_1 , m_2 , m_3 and m_4 are accessible, and show up as peaks in the k_\perp distribution. In the right panel we show the binned distribution for $m_1 = 1.25 \text{ TeV}$ together with the SM prediction with error bars corresponding to $\mathcal{L}_{\text{int}} = 1000 \text{ fb}^{-1}$. The enhancements related to radiative return to m_1, \dots, m_4 are clearly visible above the statistical noise. Another distinctive feature is that the interference between different gravitons leads to a significant enhancement of the cross section over the SM background for all values of k_\perp .

5 Summary

While the three-body cross section is lower than those of the corresponding two-body final states $\mu^+\mu^-$ and $\gamma\gamma$ by a factor of order α/π , and therefore is unlikely to be a discovery channel for massive-graviton effects, it has some distinctive features which differ from the SM and may help distinguishing between the different scenarios. First of all, the k_\perp

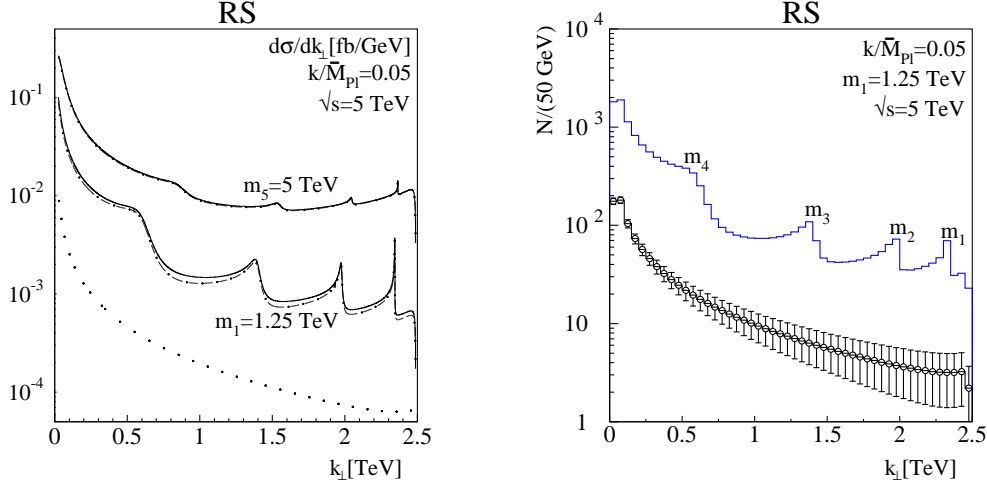


Figure 14: Photon perpendicular momentum distributions. Radiative return to the Z is excluded. Left panel: Two values of m_1 are considered, lower curves, $m_1 = 1.25$ TeV, upper curve: $m_1 \simeq 1.16$ TeV is chosen such that $m_5 = 5$ TeV. The graviton-related contributions are dash-dotted, the SM contribution is dotted. Right panel: Bin-integrated k_{\perp} distribution for $m_1 = 1.25$ TeV. The SM distribution is shown with error bars corresponding to $\mathcal{L}_{\text{int}} = 1000 \text{ fb}^{-1}$.

distribution is harder than in the SM. This applies to both the ADD and RS scenarios, and can be particularly important in the RS scenario, if the graviton has a moderately strong coupling (determined by k/\bar{M}_{Pl}). Also, the photon angular distribution can have a significant enhancement at large angles.

In the ADD scenario, where the k_{\perp} distribution is rather smooth, of the order of one year of running would be sufficient to see this hardening of the photon spectrum, for values of M_S up to about twice the c.m. energy.

In the RS scenario, ISR opens up the possibility of radiative return to the KK graviton resonances within the kinematically accessible range. This can lead to characteristic perpendicular-momentum distributions, and an increase in the cross section even when the c.m. energy is far away from any resonance.

Radiative return to the Z is also possible through ISR, but can be removed by a cut. The statistical significance of the signal can improve significantly when such a cut is included.

Here we have considered a final state with a lepton pair accompanied by a photon. It would also be of interest to consider different final states like $q\bar{q}\gamma$ (two jets and a photon) or even gluon Bremsstrahlung, $e^+e^- \rightarrow q\bar{q}g$ (three jets) in future analyses. In the latter case, the result would however be different from the case considered here (after the trivial substitutions for other coupling constants and colour factors). The reason for this difference is that the gluon can only come from the quark line, the ISR contribution would only yield photons, and therefore be of higher order compared to $e^+e^- \rightarrow$ three jets.

Acknowledgment

This research has been supported in part by the Research Council of Norway.

Appendix A: Angular- and energy-distribution functions

The angular and energy distributions of the different contributions to the cross section are in Eqs. (2.5), (2.7) and (2.11) expressed in terms of the functions $X_{AA}(x_3, \eta, \cos \theta)$ etc., where $\eta = x_1 - x_2$. It is convenient to introduce the abbreviations:

$$\begin{aligned}
z_a &= 8x_3^4 - 12x_3^2 + 12x_3 - 3, & z_j &= 2x_3^2 + 2x_3 - 1, \\
z_b &= 3(1 - 2x_3), & z_k &= 4x_3^2 + 4x_3 - 3, \\
z_c &= 2x_3^2 - 2x_3 + 1, & z_l &= 4x_3^2 - 8x_3 + 3, \\
z_d &= 4x_3^2 - 2x_3 + 1, & z_m &= 4x_3^2 - 5x_3 + 3, \\
z_e &= 2(1 - x_3)^2, & z_n &= 4x_3^2 - 20x_3 + 15, \\
z_f &= 4x_3^2 - 10x_3 + 5, & z_o &= 8x_3 - 3, \\
z_g &= 2x_3^2 - 6x_3 + 3, & z_p &= 4x_3 - 3, \\
z_h &= 4x_3^2 - 14x_3 + 7, & z_q &= 6x_3^2 - 7x_3 + 3, \\
z_i &= 8x_3^4 - 80x_3^3 + 180x_3^2 - 140x_3 + 35, & z_r &= 24x_3^2 - 40x_3 + 15.
\end{aligned} \tag{A1}$$

Here we give the functions defining the different contributions. We start with pure graviton exchange [see Eq. (2.5)]:

$$\begin{aligned}
X_{AA}(x_3, \eta, \cos \theta) &= \frac{\tilde{a}_0(x_3, \eta) + \tilde{a}_2(x_3, \eta) \cos^2 \theta + \tilde{a}_4(x_3, \eta) \cos^4 \theta}{x_3^6(1 - \cos^2 \theta)}, \\
X_{AB}(x_3, \eta, \cos \theta) &= (1 - x_3) \frac{\tilde{a}_1(x_3, \eta) \cos \theta + \tilde{a}_3(x_3, \eta) \cos^3 \theta}{x_3^5}, \\
X_{BB}(x_3, \eta, \cos \theta) &= \frac{\tilde{a}_0(x_3, \eta) + \tilde{a}_2(x_3, \eta) \cos^2 \theta + \tilde{a}_4(x_3, \eta) \cos^4 \theta}{x_3^4(1 - 2x_3)(x_3^2 - \eta^2)},
\end{aligned} \tag{A2}$$

with

$$\begin{aligned}
\tilde{a}_0(x_3, \eta) &= -\eta^4 z_a - \eta^2 x_3^2 z_b z_c + x_3^4 z_d z_e, \\
\tilde{a}_1(x_3, \eta) &= -2\eta^3 z_b + \eta x_3^2 z_b, \\
\tilde{a}_2(x_3, \eta) &= -2\eta^4 z_b z_f + 3\eta^2 x_3^2 z_b z_g - x_3^4 z_b z_c, \\
\tilde{a}_3(x_3, \eta) &= 2\eta^3 z_h - 2\eta x_3^2 z_b, \\
\tilde{a}_4(x_3, \eta) &= \eta^4 z_i - 2\eta^2 x_3^2 z_b z_f - x_3^4 z_a.
\end{aligned} \tag{A3}$$

Next we give the pure SM terms [see Eq. (2.7)]:

$$X_{C_\gamma C_\gamma}(x_3, \eta, \cos \theta) = \frac{\tilde{b}_0(x_3, \eta) + \tilde{b}_2(x_3, \eta) \cos^2 \theta}{x_3^4(1 - 2x_3)(1 - \cos^2 \theta)},$$

$$\begin{aligned}
X_{C_\gamma C_Z}(x_3, \eta, \cos \theta) &= X_{C_Z C_\gamma}(x_3, \eta, \cos \theta) = v_e v_\mu X_{C_\gamma C_\gamma} + a_e a_\mu \frac{\tilde{b}_1(x_3, \eta) \cos \theta}{x_3^4(1-2x_3)(1-\cos^2 \theta)}, \\
X_{C_Z C_Z}(x_3, \eta, \cos \theta) &= (a_e^2 + v_e^2)(a_\mu^2 + v_\mu^2) X_{C_\gamma C_\gamma} + 4a_e a_\mu v_e v_\mu \frac{\tilde{b}_1(x_3, \eta) \cos \theta}{x_3^4(1-2x_3)(1-\cos^2 \theta)}, \\
X_{C_\gamma D_\gamma}(x_3, \eta, \cos \theta) &= (1-x_3) \frac{\eta \cos \theta}{x_3^3}, \\
X_{C_\gamma D_Z}(x_3, \eta, \cos \theta) &= X_{C_Z D_\gamma}(x_3, \eta, \cos \theta) = (1-x_3) \frac{v_e v_\mu \eta \cos \theta - a_e a_\mu x_3}{x_3^3}, \\
X_{C_Z D_Z}(x_3, \eta, \cos \theta) &= (1-x_3) \frac{(a_e^2 + v_e^2)(a_\mu^2 + v_\mu^2) \eta \cos \theta - 4a_e a_\mu v_e v_\mu x_3}{x_3^3}, \\
X_{D_\gamma D_\gamma}(x_3, \eta, \cos \theta) &= \frac{\tilde{b}_0(x_3, \eta) + \tilde{b}_2(x_3, \eta) \cos^2 \theta}{x_3^2(x_3^2 - \eta^2)}, \\
X_{D_\gamma D_Z}(x_3, \eta, \cos \theta) &= X_{D_Z D_\gamma}(x_3, \eta, \cos \theta) = v_e v_\mu X_{D_\gamma D_\gamma} + a_e a_\mu \frac{\tilde{b}_1(x_3, \eta) \cos \theta}{x_3^2(x_3^2 - \eta^2)}, \\
X_{D_Z D_Z}(x_3, \eta, \cos \theta) &= (a_e^2 + v_e^2)(a_\mu^2 + v_\mu^2) X_{D_\gamma D_\gamma} + 4a_e a_\mu v_e v_\mu \frac{\tilde{b}_1(x_3, \eta) \cos \theta}{x_3^2(x_3^2 - \eta^2)}, \tag{A4}
\end{aligned}$$

with

$$\begin{aligned}
\tilde{b}_0(x_3, \eta) &= \eta^2 z_j + x_3^2 z_g, \\
\tilde{b}_1(x_3, \eta) &= -4\eta x_3 z_c, \\
\tilde{b}_2(x_3, \eta) &= \eta^2 z_g + x_3^2 z_j. \tag{A5}
\end{aligned}$$

Vector and axial couplings are normalized to $v_f = T_f - 2Q_f \sin^2 \theta_W$, $a_f = T_f$, with T_f the isospin.

Then we list the graviton-SM interference terms. First we have the pure ISR and FSR terms:

$$\begin{aligned}
X_{AC_\gamma}(x_3, \eta, \cos \theta) &= \frac{\tilde{c}_1(x_3, \eta) \cos \theta + \tilde{c}_3(x_3, \eta) \cos^3 \theta}{x_3^5(1-\cos^2 \theta)}, \\
X_{AC_Z}(x_3, \eta, \cos \theta) &= 2v_e v_\mu X_{AC_\gamma} + a_e a_\mu \frac{\tilde{c}_0(x_3, \eta) + \tilde{c}_2(x_3, \eta) \cos^2 \theta}{x_3^5(1-\cos^2 \theta)}, \\
X_{BD_\gamma}(x_3, \eta, \cos \theta) &= \frac{\tilde{c}_1(x_3, \eta) \cos \theta + \tilde{c}_3(x_3, \eta) \cos^3 \theta}{x_3^3(x_3^2 - \eta^2)}, \\
X_{BD_Z}(x_3, \eta, \cos \theta) &= 2v_e v_\mu X_{BD_\gamma} + a_e a_\mu \frac{\tilde{c}_0(x_3, \eta) + \tilde{c}_2(x_3, \eta) \cos^2 \theta}{x_3^3(x_3^2 - \eta^2)}, \tag{A6}
\end{aligned}$$

with

$$\begin{aligned}
\tilde{c}_0(x_3, \eta) &= -3\eta^2 x_3 z_c + x_3^3 z_c, \\
\tilde{c}_1(x_3, \eta) &= \eta^3 z_b - x_3^2 \eta z_b,
\end{aligned}$$

$$\begin{aligned}\tilde{c}_2(x_3, \eta) &= 9\eta^2 x_3 z_c - 3x_3^3 z_c, \\ \tilde{c}_3(x_3, \eta) &= -\eta^3 z_f + x_3^2 \eta z_b.\end{aligned}\tag{A7}$$

Finally we have the graviton-SM interference terms where one diagram is ISR and the other one is FSR. The terms with graviton exchange in the ISR diagram are:

$$\begin{aligned}X_{AD_\gamma}(x_3, \eta, \cos \theta) &= (1 - 2x_3) \frac{\tilde{d}_0(x_3, \eta) + \tilde{d}_2(x_3, \eta) \cos^2 \theta}{x_3^4}, \\ X_{AD_Z}(x_3, \eta, \cos \theta) &= v_e v_\mu X_{AD_\gamma} + a_e a_\mu (1 - 2x_3) \frac{\tilde{d}_1(x_3, \eta) \cos \theta}{x_3^4},\end{aligned}\tag{A8}$$

with

$$\begin{aligned}\tilde{d}_0(x_3, \eta) &= -\eta^2 z_k - x_3^2 z_l, \\ \tilde{d}_1(x_3, \eta) &= 4\eta x_3 z_m, \\ \tilde{d}_2(x_3, \eta) &= -\eta^2 z_n - x_3^2 z_k.\end{aligned}\tag{A9}$$

The terms with graviton exchange in the FSR diagram are:

$$\begin{aligned}X_{BC_\gamma}(x_3, \eta, \cos \theta) &= \frac{\tilde{e}_0(x_3, \eta) + \tilde{e}_2(x_3, \eta) \cos^2 \theta}{x_3^4 (1 - 2x_3)}, \\ X_{BC_Z}(x_3, \eta, \cos \theta) &= v_e v_\mu X_{BC_\gamma} + a_e a_\mu \frac{\tilde{e}_1(x_3, \eta) \cos \theta}{x_3^4 (1 - 2x_3)},\end{aligned}\tag{A10}$$

with

$$\begin{aligned}\tilde{e}_0(x_3, \eta) &= -\eta^2 z_o + x_3^2 z_p, \\ \tilde{e}_1(x_3, \eta) &= 4\eta x_3 z_q, \\ \tilde{e}_2(x_3, \eta) &= -\eta^2 z_r - x_3^2 z_o.\end{aligned}\tag{A11}$$

References

- [1] K. Akama, Lect. Notes Phys. **176**, 267 (1982) [arXiv:hep-th/0001113];
V. A. Rubakov and M. E. Shaposhnikov, Phys. Lett. B **125** (1983) 136;
E. Witten, Nucl. Phys. B **443** (1995) 85 [arXiv:hep-th/9503124];
P. Hořava and E. Witten, Nucl. Phys. B **460** (1996) 506 [arXiv:hep-th/9510209];
P. Hořava and E. Witten, Nucl. Phys. B **475** (1996) 94 [arXiv:hep-th/9603142].
- [2] I. Antoniadis, Phys. Lett. B **246** (1990) 377;
I. Antoniadis and K. Benakli, Phys. Lett. B **326**, 69 (1994) [arXiv:hep-th/9310151];
I. Antoniadis, K. Benakli and M. Quiros, Phys. Lett. B **331**, 313 (1994) [arXiv:hep-ph/9403290].

- [3] N. Arkani-Hamed, S. Dimopoulos and G. Dvali, Phys. Lett. B **429** (1998) 263 [arXiv:hep-ph/9803315].
- [4] K. R. Dienes, E. Dudas and T. Gherghetta, Phys. Lett. B **436**, 55 (1998) [arXiv:hep-ph/9803466].
- [5] N. Arkani-Hamed, S. Dimopoulos and G. Dvali, Phys. Rev. D **59** (1999) 086004 [arXiv:hep-ph/9807344].
- [6] L. Randall and R. Sundrum, Phys. Rev. Lett. **83** (1999) 3370 [arXiv:hep-ph/9905221].
- [7] L. Randall and R. Sundrum, Phys. Rev. Lett. **83** (1999) 4690 [arXiv:hep-th/9906064].
- [8] J. A. Aguilar-Saavedra *et al.* [ECFA/DESY LC Physics Working Group Collaboration], “TESLA Technical Design Report Part III: Physics at an e+e- Linear Collider,” DESY-01-011, arXiv:hep-ph/0106315;
T. Abe *et al.* [American Linear Collider Working Group Collaboration], “Linear collider physics resource book for Snowmass 2001. 1: Introduction,” in *Proc. of the APS/DPF/DPB Summer Study on the Future of Particle Physics (Snowmass 2001)* ed. N. Graf, SLAC-R-570, arXiv:hep-ex/0106055.
- [9] R. W. Assmann *et al.*, “A 3-TeV e+ e- linear collider based on CLIC technology,” SLAC-REPRINT-2000-096.
- [10] F. A. Berends and R. Kleiss, Nucl. Phys. B **177**, 237 (1981);
F. A. Berends, R. Kleiss and S. Jadach, Nucl. Phys. B **202**, 63 (1982).
- [11] E. Dvergsnes, P. Osland and N. Ozturk, Phys. Rev. D **67**, 074003 (2003) [arXiv:hep-ph/0207221]; E. Dvergsnes, P. Osland and N. Ozturk, in *Proceedings of 16th International Workshop on High Energy Physics and Quantum Field Theory (QFTHEP 2001)*, edited by M.N. Dubinin and V.I. Savrin, Moscow, Russia, Skobel'tsyn Inst. Nucl. Phys., 2001, pp. 54-63, arXiv:hep-ph/0108029.
- [12] K. m. Cheung and G. Landsberg, Phys. Rev. D **62**, 076003 (2000) [arXiv:hep-ph/9909218].
- [13] T. Han, J. D. Lykken and R. Zhang, Phys. Rev. D **59** (1999) 105006 [arXiv:hep-ph/9811350].
- [14] R. Contino, L. Pilo, R. Rattazzi and A. Strumia, JHEP **0106**, 005 (2001) [arXiv:hep-ph/0103104].
- [15] G. F. Giudice, R. Rattazzi and J. D. Wells, Nucl. Phys. B **544** (1999) 3 [arXiv:hep-ph/9811291].
- [16] J. L. Hewett, Phys. Rev. Lett. **82** (1999) 4765 [arXiv:hep-ph/9811356].

- [17] S. Hannestad and G. Raffelt, Phys. Rev. Lett. **87**, 051301 (2001) [hep-ph/0103201];
S. Hannestad and G. G. Raffelt, Phys. Rev. Lett. **88**, 071301 (2002) [hep-ph/0110067].
- [18] T. G. Rizzo, JHEP **0210** (2002) 013 [arXiv:hep-ph/0208027]; JHEP **0302**, 008 (2003) [arXiv:hep-ph/0211374].
- [19] P. Osland, A. A. Pankov and N. Paver, Phys. Rev. D **68**, 015007 (2003) [arXiv:hep-ph/0304123].
- [20] H. Davoudiasl, J. L. Hewett and T. G. Rizzo, Phys. Rev. Lett. **84** (2000) 2080 [arXiv:hep-ph/9909255]; Phys. Rev. D **63** (2001) 075004 [arXiv:hep-ph/0006041].
- [21] B. C. Allanach, K. Odagiri, M. A. Parker and B. R. Webber, JHEP **0009**, 019 (2000) [arXiv:hep-ph/0006114].